

LETTER TO THE EDITOR

$[^{12}\text{CII}]$ and $[^{13}\text{CII}]$ 158 μm emission from NGC 2024: Large column densities of ionized carbon

U. U. Graf¹, R. Simon¹, J. Stutzki¹, S. W. J. Colgan², X. Guan¹, R. Güsten³,
P. Hartogh⁴, C. E. Honingh¹, and H.-W. Hübers^{5,6}

¹ I. Physikalisches Institut der Universität zu Köln, Zùlpicher Straße 77, 50937 Köln, Germany
e-mail: graf@ph1.uni-koeln.de

² NASA Ames Research Center, Moffett Field, CA, USA

³ Max-Planck-Institut für Radioastronomie, Auf dem Hügel 69, 53121 Bonn, Germany

⁴ Max-Planck-Institut für Sonnensystemforschung, Max-Planck-Straße 2, 37191 Katlenburg-Lindau, Germany

⁵ Deutsches Zentrum für Luft- und Raumfahrt, Institut für Planetenforschung, Rutherfordstraße 2, 12489 Berlin, Germany

⁶ Institut für Optik und Atomare Physik, Technische Universität Berlin, Hardenbergstraße 36, 10623 Berlin, Germany

Received 31 January 2012 / Accepted 1 March 2012

ABSTRACT

Context. We analyze the NGC 2024 HII region and molecular cloud interface using $[^{12}\text{CII}]$ and $[^{13}\text{CII}]$ observations.

Aims. We attempt to gain insight into the physical structure of the interface layer between the molecular cloud and the HII region.

Methods. Observations of $[^{12}\text{CII}]$ and $[^{13}\text{CII}]$ emission at 158 μm with high spatial and spectral resolution allow us to study the detailed structure of the ionization front and estimate the column densities and temperatures of the ionized carbon layer in the photon-dominated region.

Results. The $[^{12}\text{CII}]$ emission closely follows the distribution of the 8 μm continuum. Across most of the source, the spectral lines have two velocity peaks similar to lines of rare CO isotopes. The $[^{13}\text{CII}]$ emission is detected near the edge-on ionization front. It has only a single velocity component, which implies that the $[^{12}\text{CII}]$ line shape is caused by self-absorption. An anomalous hyperfine line-intensity ratio observed in $[^{13}\text{CII}]$ cannot yet be explained.

Conclusions. Our analysis of the two isotopes results in a total column density of $N(\text{H}) \approx 1.6 \times 10^{23} \text{ cm}^{-2}$ in the gas emitting the $[\text{CII}]$ line. A large fraction of this gas has to be at a temperature of several hundred K. The self-absorption is caused by a cooler ($T \leq 100 \text{ K}$) foreground component containing a column density of $N(\text{H}) \approx 10^{22} \text{ cm}^{-2}$.

Key words. ISM: atoms – ISM: clouds – ISM: individual objects: NGC 2024 – photon-dominated region (PDR)

1. Introduction

NGC 2024 is a well-studied star forming region at a distance of 415 pc (Anthony-Twarog 1982) in the Orion B complex. The source consists of a dense ($n \approx 10^6 \text{ cm}^{-3}$, Schulz et al. 1991), narrow ($\approx 1'$), north-south extended molecular cloud with an embedded HII region (Krügel et al. 1982; Crutcher et al. 1986; Barnes et al. 1989), which extends several arcminutes beyond the molecular ridge in the east-west direction. The molecular material in front of the HII region is seen as a prominent dust lane in the optical. Both OH (Barnes et al. 1989) and H_2CO (Crutcher et al. 1986) absorption line measurements relative to the radio continuum indicate that this material is at a radial velocity of $v_{\text{LSR}} \approx 9 \text{ km s}^{-1}$. The bulk of the molecular gas behind the HII region is found at $v_{\text{LSR}} \approx 11 \text{ km s}^{-1}$ from observations of e.g. optically thin CO (Mauersberger et al. 1992; Graf et al. 1993; Emprechtinger et al. 2009; Buckle et al. 2010) or HCO^+ (Richer et al. 1989) lines. In the south of the HII region, a sharp ionization front delineates the boundary between the ionized and the molecular gas (e.g. MSX data in Watanabe & Mitchell 2008). This ionization front is seen edge-on in the south of the HII region, but probably also extends north in a face-on geometry along both the foreground and the background parts of the cloud.

The velocity dispersion in each of the two main parts of the cloud is small $\Delta v_{\text{LSR}} \approx 2 \text{ km s}^{-1}$, which leads to a conspicuous double-peaked line shape in many molecular emission lines. Detailed modeling of these lines (Graf et al. 1993; Emprechtinger et al. 2009) results in H_2 column densities of a few times 10^{22} cm^{-2} for the foreground component and $1-2 \times 10^{23} \text{ cm}^{-2}$ for the background component. Gas temperatures are found to be around 70 K in the background and around 30 K in the foreground, with a likely increase near the HII region interface.

In this Letter, we present $[\text{CII}]$ maps of an area near the ionization front. Our analysis concentrates on the physical properties implied by the strong $[^{13}\text{CII}]$ emission detected.

2. Observations

We observed the $^2P_{3/2} \rightarrow ^2P_{1/2}$ fine structure transition of ionized carbon (C^+) at 1900.5369 GHz (157.7 μm) (Cooksy et al. 1986) toward the NGC 2024 (Orion B) molecular cloud. The measurements were made on Nov. 8, 2011 using the German REceiver for Astronomy at Terahertz frequencies (GREAT)¹

¹ GREAT is a development by the MPI für Radioastronomie und KOSMA/Universität zu Köln, in cooperation with the MPI für Sonnensystemforschung and the DLR Institut für Planetenforschung.

(Heyminck et al. 2012) on the Stratospheric Observatory For Infrared Astronomy (SOFIA; Young et al. 2012).

The receiver noise temperature during the observations was approximately 4000 K (SSB). With a zenith opacity of 0.03–0.07, the system temperature was lower than 4500 K (SSB). The beam size was 16". The velocity resolution before smoothing was 33 m/s.

We mapped a $192'' \times 144''$ area in total power on-the-fly mode. Both the sampling distance along the scan direction and the scan spacing were 6". The map was centered on $(\alpha, \delta) = (05^{\text{h}}41^{\text{m}}45^{\text{s}}.20, -01^{\circ}55'45''.0)$ (J2000) using an off-position at $(05^{\text{h}}41^{\text{m}}36^{\text{s}}.30, -02^{\circ}05'00''.0)$. According to Jaffe et al. (1994) and confirmed by a comparison measurement to a second, far-away off-position, no [CII] emission could be detected at this position.

The measurements were calibrated using the procedure outlined in Guan et al. (2012). Instead of the main beam efficiency of 0.51 (Heyminck et al. 2012), we used a value of 0.58 to account for the non-negligible coupling of the first side lobes to an extended source, as derived from a model of the diffraction pattern. A linear baseline was subtracted from each spectrum.

3. Results

Figure 1 shows the measured [CII] intensity distribution integrated over the velocity interval 5–15 km s⁻¹. The emission agrees remarkably well with the 8 μm MSX data (Price et al. 2001; Watanabe & Mitchell 2008), which traces the UV-heated dust in the interface between the HII region and the molecular cloud. Only the embedded MSX source just north of the map center is not very prominent in the [CII] data. The emission peaks along the southern rim of the HII region, where the interface is seen edge-on in a sharp ionization front.

The intensity distribution does not reflect the distribution of the molecular material located in a roughly north-south elongated molecular ridge – outlined by the FIR peaks in Fig. 1.

Averaged over a 60" diameter, we obtain a peak surface brightness of 4.4×10^{-3} erg cm⁻² s⁻¹ sr⁻¹, in reasonable agreement with KAO and ISO data (Jaffe et al. 1994; Giannini et al. 2000).

3.1. [¹³CII] distribution

With a velocity span of ± 100 km s⁻¹, the spectra also cover the three hyperfine structure components of the [¹³CII] transition (v_{LSR} -offsets -65.2, 11.2, 63.2 km s⁻¹, Cooksy et al. 1986) (Fig. 3). If we co-add the velocity ranges [-60, -50], [19, 25], and [70, 80] km s⁻¹ (taking into account the systemic velocity), we find emission with a similar spatial distribution as the main isotope (Fig. 1).

The [¹³CII] emission is only prominent in a crescent-shaped area following the edge-on ionization front, where column densities are highest. The peak emission coincides with the [¹²CII] emission maximum, but the [¹³CII] intensity falls off more rapidly, both to the HII region side (north) and to the molecular cloud side (south). The FWHM of the [¹³CII] emission zone is $\approx 1'$, corresponding to a linear size of ≈ 0.1 pc.

3.2. [¹²CII] channel maps

The [CII] emission is separated into two distinct velocity components, which show up as two peaks in most spectra (Fig. 3). Figure 2 presents channel maps of 1 km s⁻¹ wide velocity bins

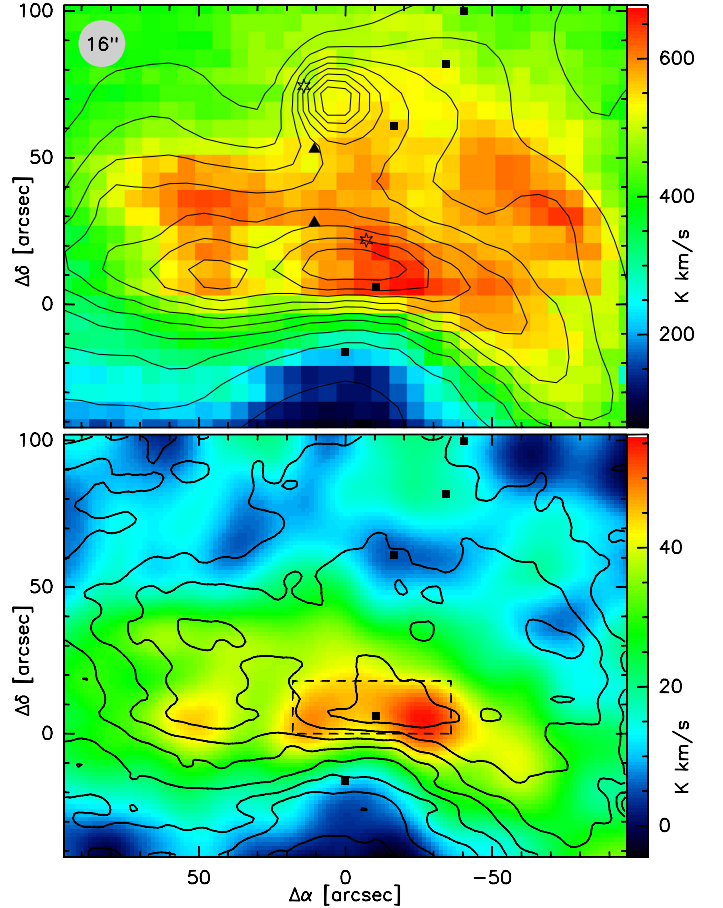


Fig. 1. *Top:* integrated (5–15 km s⁻¹) [CII] intensity map of NGC 2024 (color code). Comparison data: MSX Band A (8.28 μm) (contours), 6 cm continuum peaks (triangles) (Crutcher et al. 1986), 1.3 mm continuum emission clumps FIR2 to FIR6 (Mezger et al. 1988), and embedded infrared point sources IRS2 (Grasdalen 1974) and IRS3 (Barnes et al. 1989) (stars). *Bottom:* overlay of the [¹³CII] (color coded) and the [¹²CII] integrated intensities (contours: 100 K km s⁻¹ to 625 K km s⁻¹ in steps of 75 K km s⁻¹). The [¹³CII] map has been smoothed to a resolution of 25". The dashed box outlines the area of strong emission that was used in the analysis of Sect. 4.

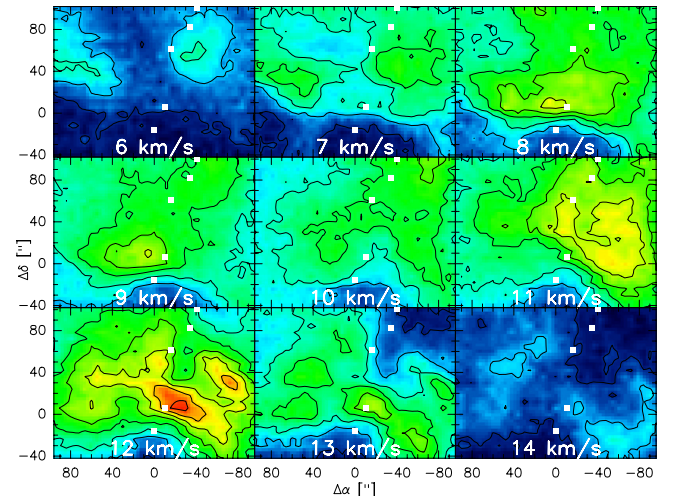


Fig. 2. [¹²CII] channel maps of 1 km s⁻¹ wide velocity channels spaced by 1 km s⁻¹. Panels are labeled by their center velocity. The markers denote the positions of the clumps FIR2 to FIR6 (Mezger et al. 1988). Contour levels are from 10 K km s⁻¹ to 150 K km s⁻¹ in steps of 20 K km s⁻¹.

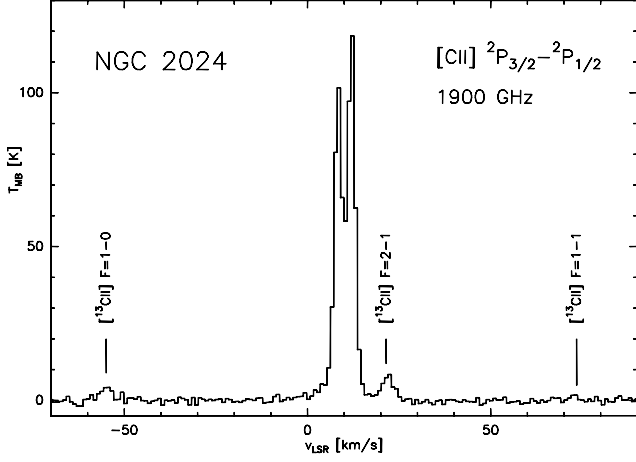


Fig. 3. Spectrum averaged over the area outlined in Fig. 1 with marks indicating the predicted velocities of the [^{13}CII] hyperfine components (Cooksy et al. 1986).

ranging from 6 km s^{-1} to 14 km s^{-1} . The maps clearly show the two main velocity peaks, which are predominant throughout most of the source. The low velocity peak dominates the 8–9 km s^{-1} panels, the high velocity peak being clearly visible at 11 and 12 km s^{-1} . The local minimum in the 10 km s^{-1} velocity bin around FIR5 coincides with the peak of the integrated intensity map (Fig. 1).

There appears to be an anticorrelation between the low velocity peak and the high velocity peak. The relatively high intensities found at 9 km s^{-1} west of FIR2 to FIR4 and east of FIR5 correspond to areas of weak emission at 12–13 km s^{-1} .

4. Discussion

For the data analysis, the interpretation of the two velocity peaks of the spectra is crucial. Although the [CII] peaks – at velocities of $\sim 8.4 \text{ km s}^{-1}$ and $\sim 12 \text{ km s}^{-1}$ – are slightly offset from the two emission components in the optically thin lines of very rare CO isotopes (9.2 km s^{-1} and 11.2 km s^{-1} , Graf et al. 1993), it seems reasonable to assume that the [CII] line may also be caused by two emission components and not by self-absorption. The [^{13}CII] measurement allows us to clearly distinguish between these two possibilities.

4.1. [^{13}CII] spectrum

To obtain a high signal-to-noise spectrum to analyze the isotopic line, we averaged the spectra within a rectangular area encompassing the peak of the [^{13}CII] emission (marked by a dashed box in Fig. 1). The resulting spectrum is shown in Fig. 3. In Fig. 4, we compare the line profile of the [^{12}CII] line to the three hyperfine satellites of [^{13}CII].

It is immediately obvious that the isotopic line only shows a single peak. Thus, either a) only one of the two velocity components seen in [^{12}CII] has a sufficiently high column density to produce measurable [^{13}CII] emission, or b) the shape of the [^{12}CII] is produced by a warm broad background component shadowed by a narrow cooler foreground component. Explanation a) would imply that there is an error in the rest frequencies of $\geq 10 \text{ MHz}$, clearly beyond the confidence limits of Cooksy et al. (1986) and in contrast to the good agreement found in recent HIFI measurements toward the Orion bar (Ossenkopf et al. 2011). Thus, if we accept the rest frequencies

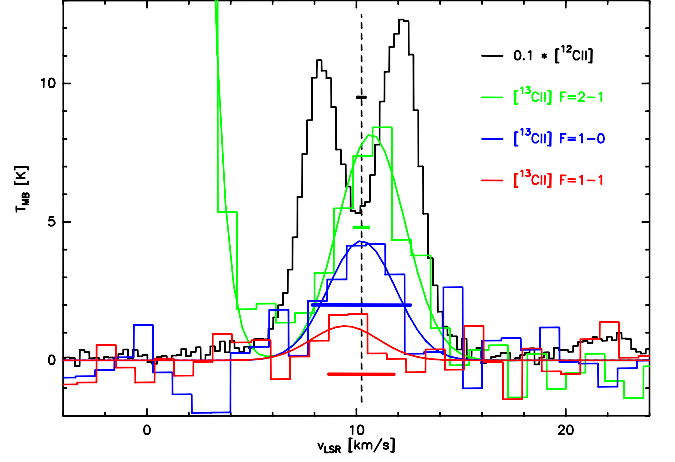


Fig. 4. Spectrum of Fig. 3 replotted on a common v_{LSR} scale and overlaid by the model fit (see text and Table 1). The dashed line marks the center velocity of the [^{12}CII] background component. Horizontal bars indicate the uncertainty in the rest frequencies. The [^{12}CII] has been divided by ten.

Table 1. Parameters of the fit to the spectrum of Fig. 4.

	[^{12}CII]		[^{13}CII]		
	Emiss.	Absorb.	1 \rightarrow 0	2 \rightarrow 1	1 \rightarrow 1
T_{MB} [K]	[400]	-352.5	4.3	8.2	(1.2)
v_{LSR} [km s^{-1}]	10.26	10.20	-54.9	21.9	(72.7)
Δv_{LSR} [km s^{-1}]	3.8	2.7	[3.8]	[3.8]	[3.8]
δv_{LSR} [km s^{-1}]	–	–	-65.2	11.7	(62.4)
Rel. intens.	–	–	{-65.2}	{11.2}	{63.2}
	–	–	0.31	0.60	(0.09)
	–	–	{0.356}	{0.444}	{0.200}

Notes. δv_{LSR} denotes the velocity offset of the [^{13}CII] hyperfine satellites to the [^{12}CII] background component. Bracket symbols: []: fixed value; {}: literature value (Cooksy et al. 1986); (): weakly constrained value.

to their published accuracy, we are forced to the conclusion that the [^{12}CII] line profile is caused by self-absorbed strong background emission centered at $v_{\text{LSR}} \approx 10 \text{ km s}^{-1}$.

Self-absorption in the [^{12}CII] line offers a quite natural explanation of the anticorrelation observed in the spatial distribution of the two velocity peaks: a velocity shift of the absorbing component with respect to the background component shifts the observed line intensity from one velocity peak to the other.

That the highest contrast between the 10 km s^{-1} dip and the 8 km s^{-1} and 12 km s^{-1} peaks is found in an area of known strong foreground absorption (Crutcher et al. 1986; Barnes et al. 1989) also strengthens this interpretation. Radio recombination lines of carbon (Krügel et al. 1982, and reference therein) are also mostly near 10 km s^{-1} .

The discrepancy between the CO velocities and the self-absorbed [CII] emission indicates that the simple source model with only two velocity components may underestimate the kinematic complexity of the source.

4.2. Hyperfine line ratios

Figure 4 includes the result of a five-component Gaussian fit to the spectrum. The first two components model the main isotope (fit not shown in Fig. 4) as an emissive and an absorptive component. The remaining three components fit the three hyperfine lines, where the line width is kept fixed and equal to the width

of the broad background component. Table 1 lists the fit results and compares the parameters of the $[^{13}\text{CII}]$ hyperfine satellites to the literature values.

For the two stronger hyperfine components, the velocities are within 0.5 km s^{-1} (3 MHz) of the predicted values. The signal-to-noise ratio of the $F = 1 \rightarrow 1$ component is too low to make a firm statement. The predicted line strength ratio, however, is not reproduced by our measurement. The $(F = 2 \rightarrow 1)/(F = 1 \rightarrow 0)$ intensity ratio should be 1.25, but is found to be 1.9. A similar discrepancy was also found by Ossenkopf et al. (2011).

Obviously it cannot be ruled out that an as yet unknown emission line may coincide with the $F = 2 \rightarrow 1$ line, leading to excess emission at this velocity. However, strong spectral lines at these wavelengths are so rare that this seems highly unlikely. At the moment, we can only speculate that the anomalous hyperfine ratio may be due to some non-LTE excitation mechanism, possibly caused by hyperfine-selective radiative pumping by emission lines of the main isotope at shorter wavelengths.

4.3. Physical conditions

The integrated intensity in the three hyperfine components adds up to 52 K km s^{-1} , which – in the high density limit ($n > 3000 \text{ cm}^{-3}$) – converts into a column density $N(^{13}\text{C}^+) = 2.6 \times 10^{17} \text{ cm}^{-2}$ (Crawford et al. 1985). Assuming standard abundance ratios², this corresponds to $N(^{12}\text{C}^+) = 1.6 \times 10^{19} \text{ cm}^{-2}$ and a total hydrogen column density of $N(\text{H}) = 1.6 \times 10^{23} \text{ cm}^{-2}$ in the gas emitting the $[\text{CII}]$ lines, if all the carbon is ionized.

Owing to the foreground absorption, the intrinsic $[^{12}\text{CII}]$ emission is not constrained well. The background emission line component requires temperatures of several 100 K, with 165 K being a hard lower limit³. For a gas temperature of e.g. 400 K, the $[^{12}\text{CII}]$ line would be almost optically thick ($\tau \approx 2.4$) with an intrinsic line temperature of $T_{\text{MB}}([^{12}\text{CII}], \text{background}) \approx 325 \text{ K}$.

Standard spherical photon-dominated region (PDR) models (Störzer et al. 1996; Röllig et al. 2006) of even the most extreme single clumps fall short by about one order of magnitude of reproducing this high line intensity and large column density of ionized carbon. It is plausible that the edge-on geometry of the ionization front may significantly boost the total column density. Thus, an equivalent of ten extreme clumps would be required to model the observed emission. Similarly, in a clumpy PDR model (Cubick et al. 2008), where the amount of material exposed to UV radiation is drastically higher, the predicted $[\text{CII}]$ emission is much stronger. For instance, a typical model⁴ with a total mass within the beam of $1 M_{\odot}$, a radiation field of $\chi = 10^3$ and an average density of 10^6 cm^{-3} can produce the observed $[^{13}\text{CII}]$ intensity. These values correspond to a hydrogen column density of $\approx 10^{23} \text{ cm}^{-2}$, in agreement with the above estimate.

With the absorption dip reaching down to 53 K (Fig. 4), the temperature in the foreground gas is limited to $T_{\text{FG}} \leq 90 \text{ K}$ ⁵. The optical depth derived for the foreground gas is $\tau_{\text{FG}} \geq 1$, where the exact value depends on the assumptions made about the temperatures. If we accept an intrinsic main beam brightness temperature of 325 K for the background component, the column density of ionized carbon in the absorbing layer needs to be $N(\text{C}^+) \geq 10^{18} \text{ cm}^{-2}$ for any gas temperature above 40 K.

² Assumed abundances: $^{12}\text{C}/^{13}\text{C} = 60$; $^{12}\text{C}/\text{H} = 10^{-4}$.

³ Owing to the Rayleigh-Jeans correction, the peak T_{MB} of 125 K (Fig. 4) requires gas temperatures of $\geq 165 \text{ K}$.

⁴ The single line data are insufficient to fully constrain a model.

⁵ Rayleigh-Jeans correction: $T_{\text{R,J}}(90 \text{ K}, 1900 \text{ GHz}) = 53 \text{ K}$.

5. Conclusions

We have observed both $[^{12}\text{CII}]$ and $[^{13}\text{CII}]$ emission toward NGC 2024. The spatial distribution of the emission follows the $8 \mu\text{m}$ continuum emission, tracing the interface between the HII region and the molecular cloud. The isotopic line emission detected from an area near the ionization front implies that:

- the double-peaked spectrum of the $[^{12}\text{CII}]$ line is due to strong background emission absorbed by cooler foreground gas at the same velocity;
- the kinematic signature of the ionized gas differs from that of the molecular gas as traced by rare isotopes of CO;
- the total hydrogen column density of warm gas at several hundred Kelvin traced by the $[\text{CII}]$ emission amounts to $\geq 10^{23} \text{ cm}^{-2}$, suggesting that the interface is highly clumpy;
- the strong foreground absorption implies a hydrogen column density $\geq 10^{22} \text{ cm}^{-2}$ of gas at temperatures below 100 K;
- The measured intensity ratio of the hyperfine components does not match the theoretical value, suggesting that there is some contribution from a non-LTE excitation effect

Acknowledgements. We thank Volker Ossenkopf and Markus Röllig for useful discussions. We also thank the SOFIA engineering and operations teams whose tireless support and good-spirit teamwork has been essential for the GREAT accomplishments during Early Science, and say Herzlichen Dank to the DSI telescope engineering team. This work is based on observations made with the NASA/DLR Stratospheric Observatory for Infrared Astronomy. SOFIA Science Mission Operations are conducted jointly by the Universities Space Research Association, Inc., under NASA contract NAS2-97001, and the Deutsches SOFIA Institut under DLR contract 50 OK 0901.

References

- Anthony-Twarog, B. J. 1982, *AJ*, 87, 1213
- Barnes, P. J., Crutcher, R. M., Biegging, J. H., Storey, J. W. V., & Willner, S. P. 1989, *ApJ*, 342, 883
- Buckle, J. V., Curtis, E. I., Roberts, J. F., et al. 2010, *MNRAS*, 401, 204
- Cooksy, A. L., Blake, G. A., & Saykally, R. J. 1986, *ApJ*, 305, L89
- Crawford, M. K., Genzel, R., Townes, C. H., & Watson, D. M. 1985, *ApJ*, 291, 755
- Crutcher, R. M., Henkel, C., Wilson, T. L., Johnston, K. J., & Biegging, J. H. 1986, *ApJ*, 307, 302
- Cubick, M., Stutzki, J., Ossenkopf, V., Kramer, C., & Röllig, M. 2008, *A&A*, 488, 623
- Emprechtinger, M., Wiedner, M. C., Simon, R., et al. 2009, *A&A*, 496, 731
- Giannini, T., Nisini, B., Lorenzetti, D., et al. 2000, *A&A*, 358, 310
- Graf, U. U., Eckart, A., Genzel, R., et al. 1993, *ApJ*, 405, 249
- Grasdalen, G. L. 1974, *ApJ*, 193, 373
- Guan, X., Stutzki, J., Graf, U. U., et al. 2012, *A&A*, 542, L4
- Heyminck, S., Graf, U. U., Güsten, R., et al. 2012, *A&A*, 542, L1
- Jaffe, D. T., Zhou, S., Howe, J. E., et al. 1994, *ApJ*, 436, 203
- Krögel, E., Thum, C., Pankonin, V., & Martin-Pintado, J. 1982, *A&AS*, 48, 345
- Mauersberger, R., Wilson, T. L., Mezger, P. G., Gaume, R., & Johnston, K. J. 1992, *A&A*, 256, 640
- Mezger, P. G., Chini, R., Kreysa, E., Wink, J. E., & Salter, C. J. 1988, *A&A*, 191, 44
- Ossenkopf, V., Röllig, M., Fuente, A., et al. 2011, in *IAU Symp.* 280, 280
- Price, S. D., Egan, M. P., Carey, S. J., Mizuno, D. R., & Kuchar, T. A. 2001, *AJ*, 121, 2819
- Richer, J. S., Hills, R. E., Padman, R., & Russell, A. P. G. 1989, *MNRAS*, 241, 231
- Röllig, M., Ossenkopf, V., Jeyakumar, S., Stutzki, J., & Sternberg, A. 2006, *A&A*, 451, 917
- Schulz, A., Güsten, R., Zylka, R., & Serabyn, E. 1991, *A&A*, 246, 570
- Störzer, H., Stutzki, J., & Sternberg, A. 1996, *A&A*, 310, 592
- Watanabe, T., & Mitchell, G. F. 2008, *AJ*, 136, 1947
- Young, E. T., Becklin, E. E., Marcum, J. M., et al. 2012, *ApJ*, 749, L17